Journal of Hazardous Materials 445 (2023) 130552

Contents lists available at ScienceDirect

Journal of Hazardous Materials

journal homepage: www.elsevier.com/locate/jhazmat

Defective SO_3H-MIL-101(Cr) for capturing different cationic metal ions: Performances and mechanisms

Xueying Ren [a,b], Chong-Chen Wang [a,b,*], Ya Li [a,b], Peng Wang [a,b], Shijie Gao [a,b]

[a] Beijing Key Laboratory of Functional Materials for Building Structure and Environment Remediation, Beijing University of Civil Engineering and Architecture, Beijing 100044, China

[b] Beijing Energy Conservation & Sustainable Urban and Rural Development Provincial and Ministry Co-construction Collaboration Innovation Center, Beijing University of Civil Engineering and Architecture, Beijing 100044, China

HIGHLIGHTS

- Defective SO_3H-MIL-101(Cr) with abundant vacancies was obtained.
- SS-SO_3H-MIL-101(Cr)-X exhibited adsorption activity toward various metal cations.
- The sorption mechanisms were clarified via characterizations and DFT calculations.

GRAPHICAL ABSTRACT

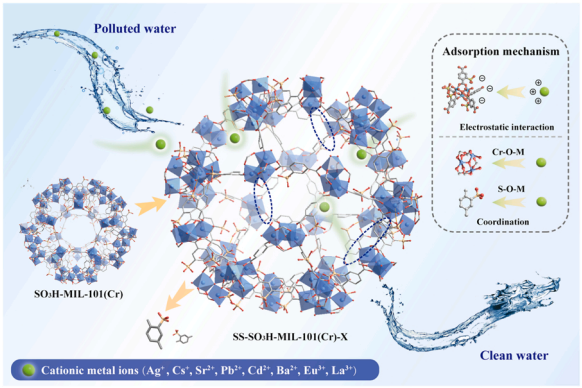

ARTICLE INFO

Editor: Arturo J Hernandez-Maldonado

Keywords:
SO_3H-MIL-101(Cr)
Defect
Heavy metal pollution
Adsorption
Mechanism

ABSTRACT

For broad-spectrum adsorption and capture toward cationic metal ions, a facile strategy was adopted to fabricate defective SO_3H-MIL-101(Cr) (SS-SO_3H-MIL-101(Cr)-X, X = 2, 3, 4) with enhanced vacancies using seignette salt (SS) as the modulating agent. The boosted adsorption performances of SS-SO_3H-MIL-101(Cr)-X toward eight different ions, including Ag^+, Cs^+, Pb^{2+}, Cd^{2+}, Ba^{2+}, Sr^{2+}, Eu^{3+} and La^{3+} in both individual component and mixed component systems, could be ascribed to the effective mass transfer resulting from the exposure of defective sites. Especially, the optimal SS-SO_3H-MIL-101(Cr)−3 could remove all the selected metal cations to below the permissible limits required by the World Health Organization (WHO) in the continuous-flow water treatment system. Furthermore, SS-SO_3H-MIL-101(Cr)−3 exhibited good adsorption capacity (189.6 $mg{\cdot}g^{-1}$) toward Pb^{2+} under neutral condition and excellent desorption recirculation performance (removal efficiency > 95% after 5 cycles). Moreover, the adsorption mechanism involved the electrostatic adsorption and coordinative interactions resulting from complexation between the adsorption active sites and targeted cations (like Cr-O-M and S-O-M), which were explored systematically via both X-ray photoelectron spectroscopy (XPS) determination

* Corresponding author at: Beijing Key Laboratory of Functional Materials for Building Structure and Environment Remediation, Beijing University of Civil Engineering and Architecture, Beijing 100044, China.

E-mail addresses: wangchongchen@bucea.edu.cn, chongchenwang@126.com (C.-C. Wang).

https://doi.org/10.1016/j.jhazmat.2022.130552
Received 6 October 2022; Received in revised form 17 November 2022; Accepted 3 December 2022
Available online 6 December 2022

and density functional theory (DFT) calculations. Overall, this work provided guidance for modulating SS-SO_3H-MIL-101(Cr)-X to promote its potential application in widespread metal cations removal from wastewater.

1. Introduction

The comprehensive utilization of metallic materials resulted into various heavy metal pollutants in water environment (Suksabye et al., 2012). The lead, cadmium, and barium ions are hazardous contaminants with teratogenic, carcinogenic, and mutagenic properties, which can migrate with water to be accumulated in organisms (Du et al., 2017; Younis et al., 2021). Furthermore, some precious metal ions and rare earth metals like silver or europium can also be extensively detected in industrial wastewater, which are considered recyclable substances due to their scarcity and high cost (Nakhjiri et al., 2022). Therefore, both the elimination of toxic and harmful metals and the recovery of valuable metals are of great significance to conserve resources and the protect the environment (Wang et al., 2016).

Various wastewater treatment approaches have been developed and practiced to remove metal ions from wastewater, like chemical reduction (Zhao et al., 2022), coagulation (El Samrani et al., 2008), precipitation (Navarro et al., 2005), ion-exchange (Du et al., 2017), membrane filtration (Llanos et al., 2010), and adsorption (Ma et al., 2021). Compared with others, adsorption is regarded as one of the most promising techniques due to its facile operation, low energy consumption, and minimal or free secondary pollution (Bolisetty et al., 2019). Some generally used adsorbents like activated carbons (AC) (Hadi et al., 2015), metal oxides/sulfides (He et al., 2017; Kobielska et al., 2018), and exchange resins (Rychkov et al., 2021) suffered from some shortcomings like poor sorption capacity, and low regeneration performance (Chang et al., 2021).

Metal-organic frameworks (MOFs) with controlled structures, large surface areas, tunable micropores, and multiple adsorption sites could provide favorable surroundings for the interactions between sorption sites and metal ions in the framework (Gao et al., 2021; Wang et al., 2022a, 2022b). The existing MOF adsorbents display the universal trait of specific capture for metal ions, which could be widely applied in pollutant removal and resource recovery (Guan et al., 2019; Zorainy et al., 2021). Nevertheless, the species of heavy metals in industrial wastewater are complicated and diverse (Peng et al., 2018). Therefore, the development of broad-spectrum sorbents with uniformly distributed sorption sites is highly needed.

In recent years, SO_3H-MIL-101(Cr) has been extensively investigated as an efficient adsorbent for capturing cationic organic dyes (Luo et al., 2017), naphthalenesulfonic acid (Zhao et al., 2018), fluoroquinolone antibiotics (Guo et al., 2019). The SO_3H-MIL-101(Cr) inherits the structural advantage of most MOFs while overcome their disadvantages like poor chemical stability. Specifically, the introduction of negatively charged -SO_3H groups could provide additional adsorption sites for capturing cationic pollutants (Yoo et al., 2023). To further improve the adsorption performance, it is expected to take advantage of defect engineering for creating more open spaces and active adsorption sites. In the process of introducing defects, the modulator generally acts on increasing adsorption capacity in two aspects: (i) to increase both the specific surface area and the pore volume of MOFs adsorbents for creating more sorption sites resulting from the missing linkers (Li et al., 2022b), (ii) to influence the nucleation behaviors of MOFs (Jiang et al., 2021a; Kabtamu et al., 2020). In our previous study, the Zr-MOFs like NH_2-UiO-66 were modulated by seignette salt to obtain hierarchical pores and abundant vacancies, which displayed excellent adsorption activity toward Pb^{2+} (Li et al., 2022a). Recently, researchers focused their attention to fabricate the defective Zr-MOFs like UiO-66 or NH_2-UiO-66 via the coordination adjustment strategy (Jiang et al., 2021a). However, there are few reports introducing defect sites into Cr-MOFs to enhance the sorption ability toward environmental pollutants.

To tackle this need, hereon, we adopted a facile, environmentally friendly post-modification strategy to modulate SO_3H-MIL-101(Cr) for obtaining effective adsorbents with more accessible chelating sites and high affinity to achieve broad-spectrum adsorption toward eight different heavy metal ions. Particularly, in the single-component system, the defective SS-SO_3H-MIL-101(Cr)− 3 showed good adsorption performance towards all the metal cations in both batch sorption and breakthrough processes. More importantly, the multi-component experiments demonstrated that the SS-SO_3H-MIL-101(Cr)− 3 had enormous potential for capturing multiple metal cations in practical industrial wastewater. In addition, this defective SS-SO_3H-MIL-101(Cr)− 3 adsorbent can be easily regenerated without noticeable adsorption capacity decrease. The results from this study can provide adsorption behavior and mechanism insights into the defective Cr-MOF for metal cation pollutants, further expanding the application of defective MOFs in wastewater treatment field.

2. Experimental

The information of chemicals/reagents, analytical methods and the used instruments are provided in the Supplementary Information (**SI**).

2.1. Preparation of SO_3H-MIL-101(Cr) and SS-SO_3H-MIL-101(Cr)-X

The SO_3H-MIL-101(Cr) was prepared via the reported hydrothermal approach with a little modification (Zhou et al., 2014). 3.75 mmol (1.006 g) of 2-sulfoterephthalic acid and 3.75 mmol (0.3750 g) of CrO_3 were ultrasonically dissolved in an aqueous 15.0 mL 0.54% HCl solution. The obtained mixture was transferred into a 25.0 mL autoclave lined with Teflon, which was heated in an oven at 180 ℃ for 6 d. After collection, the obtained green precipitates were washed to eliminate the residual reactant, and dried in a vacuum at 60 ℃ for 8 h (88.1% yield calculated from input 2-sulfoterephthalic acid).

The as-obtained SO_3H-MIL-101(Cr) (100.0 mg) was dispersed in 50.0 mL aqueous solution of seignette salt (2 mmol, 3 mmol, and 4 mmol, respectively) at 60 °C for 10 h to obtain defective SO_3H-MIL-101(Cr) (SS-SO_3H-MIL-101(Cr)-X, X = 2, 3, and 4, respectively), in which the yield of SS-SO_3H-MIL-101(Cr)− 2, SS-SO_3H-MIL-101(Cr)− 3, SS-SO_3H-MIL-101(Cr)− 4 were 48.12%, 43.89% and 30.41%, respectively (yield based on SO_3H-MIL-101(Cr)).

2.2. Batch adsorption experiments

To explore the adsorption behaviors of SS-SO_3H-MIL-101(Cr)-X particles toward cationic metal ions, Pb^{2+} was selected as target pollutant model in the batch sorption experiments. For kinetic experiments, the as-obtained SS-SO_3H-MIL-101(Cr)-X particles (20.0 mg) were put into a 100.0 mL Pb^{2+} solutions with concentrations in the range from 5.0 to 100.0 mg·L^{-1} at pH = 5.6, which was stirred at 170 rpm under 298 K for 2 h. The isotherm experiments were conducted with the same conditions under 288 K, 298 K and 308 K, respectively. During the shaking process, the supernatant was filtered using a 0.22 μm springe filter to determine the residual Pb^{2+} concentration using the inductively coupled plasma-optical emission spectrometry (ICP-OES, ICP-500, Focused Photonics Inc).

To examine the regeneration efficacy of SS-SO_3H-MIL-101(Cr)-X, 20.0 mg of the used adsorbent was regenerated by being washed with 10 mL of 1% HNO_3 solution at 298 K for 5 min

2.3. Column adsorption experiments

The fixed-bed column experiments were carried out using solid phase extraction (SPE) column (<*l*> = 80 mm and <*d*> = 15 mm), in which the SPE column was packed with 300.0 mg of the selected adsorbent to form the bed volume of 10 mL. The solution containing 5 $mg{\cdot}L^{-1}$ selected metal cation was pumped through the SPE column with flow rate of 0.5 $mL{\cdot}min^{-1}$ via a peristaltic pump (BT-300S). During the sorption process, 2.5 mL effluent was collected regularly to test the concentrations of residual metal ion and the leached Cr from the adsorbent by the ICP-OES.

3. Results and discussion

3.1. Characterizations of SS-SO_3H-MIL-101(Cr)-X

The powder X-ray diffraction (PXRD) patterns of series defective SS-SO_3H-MIL-101(Cr)-X and the pristine SO_3H-MIL-101(Cr) particles matched well with the simulated PXRD patterns from the single crystal data (CCDC 605510) (Férey et al., 2005). However, as depicted in Fig. 1**a**, the peak intensity ($2\theta = 9.04$) corresponding to the (753) facet of SO_3H-MIL-101(Cr) decreased with the increasing seignette salt concentration, revealing a gradual increase in defect ratio. The scanning electron microscopy (SEM) was used to confirm the structure of SS-SO_3H-MIL-101(Cr)-X and SO_3H-MIL-101(Cr). It was observed that these four samples exhibited blocky morphology with particle sizes ranging from 100 to 400 nm, in which no significant morphology change could be observed after modification (Fig. 1**b**). Meanwhile, Fig. S1

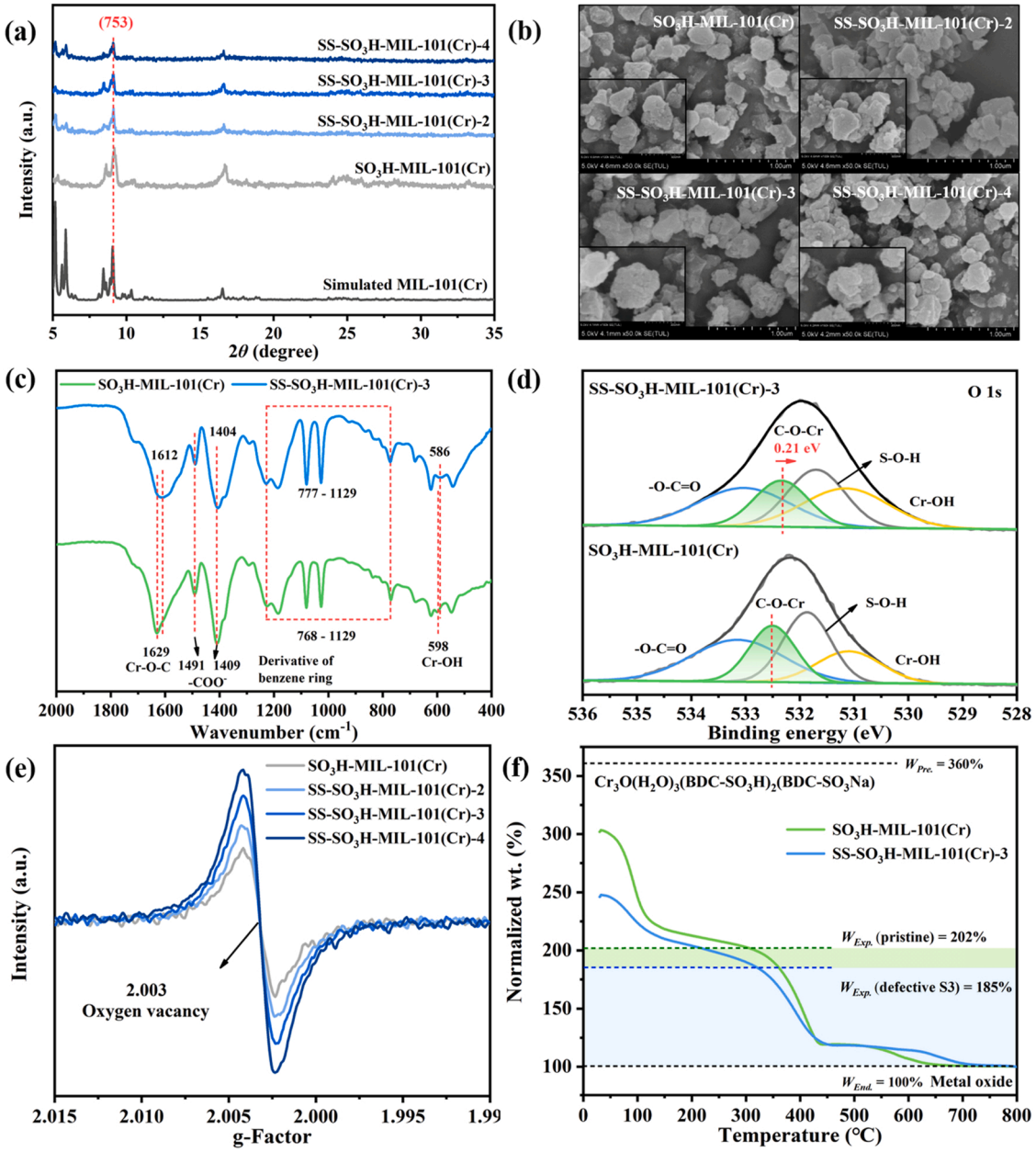

Fig. 1. (a) The PXRD patterns, (b) SEM images of SO_3H-MIL-101(Cr) and series SS-SO_3H-MIL-101(Cr)-X, (c) FTIR spectra and (d) the XPS spectra of O 1 s of pristine SO_3H-MIL-101(Cr) and SS-SO_3H-MIL-101(Cr)− 3, (e) the EPR spectra of SO_3H-MIL-101(Cr) and series SS-SO_3H-MIL-101(Cr)-X, (f) TGA curves of pristine SO_3H-MIL-101(Cr) and SS-SO_3H-MIL-101(Cr)− 3.

showed that both SO_3H-MIL-101(Cr) and SS-SO_3H-MIL-101(Cr)− 3 displayed the similar lattice fringe of ca. 0.220 nm corresponding to the (753) facet (Chen et al., 2016), suggesting the good crystallinity of SS-SO_3H-MIL-101(Cr)− 3 after the modulation process.

The defective structures of SS-SO_3H-MIL-101(Cr)-X were examined by Fourier transform infrared (FTIR) spectra and X-ray photoelectron spectra (XPS). Comparing the FTIR spectra of SS-SO_3H-MIL-101(Cr)− 3 to those of SO_3H-MIL-101(Cr) (Fig. 1**c**), the peaks at 1612 and 1404 cm^{-1} corresponding to asymmetric and symmetric stretching of carboxylic groups showed a slight blue shift, indicating the occurrence of decarboxylation during the seignette salt treatment (Sun et al., 2014). Meanwhile, the peaks in the range 777–1129 cm^{-1} corresponding to the derivatives of the benzene ring showed that the modulation caused decarboxylation and the SO_3H-BDC was removed (Mortazavi et al., 2019). Additionally, the weakening of Cr-O-C bond (1612 cm^{-1}) intensity indicated that C-O bonds may be broken. This is consistent with the results of the XPS in Fig. 1**d**, in which the area ratios of the Cr-O-C band (532.55 eV) belonged to pristine SO_3H-MIL-101(Cr) decreased from 21.94% to 19.68% of SS-SO_3H-MIL-101(Cr)− 3 (532.34 eV) (Ullah et al., 2019). The splitting of Cr-O-C bonds might lead to the formation of oxygen vacancies and coordinatively unsaturated chromium atoms. Correspondingly, the area ratio of Cr-OH peak (531.1 eV) in the O 1 s signal (Fig. 1**d**) demonstrated a significant increase from 17.32% of the pristine SO_3H-MIL-101(Cr) to 26.32% of SS-SO_3H-MIL-101(Cr)− 3 (Ran et al., 2022).

The EPR was used to explore the influence of seignette salt concentration on the structure characteristics of SO_3H-MIL-101(Cr) and SS-SO_3H-MIL-101(Cr)-X. As depicted in Fig. 1**e**, the EPR spectrum of the SS-SO_3H-MIL-101(Cr)− 3 displayed a peak at *g* being 2.003 (Zhang et al., 2021b), indicating the existence of a significant oxygen vacancies in the framework (Hong et al., 2009). Noticeably, upon increasing the concentration of seignette salt, the intensities of the peak at g = 2.003 increased noticeably, implying that more adsorption sites were exposed (Li et al., 2022a). These findings proposed that the defect structure of SS-SO_3H-MIL-101(Cr)-X was originated from SO_3H-BDC decomposition.

Thermogravimetric analyses (TGA) were adopted to further study the defects in SS-SO_3H-MIL-101(Cr)-X and quantify the number of the missing linkers, in which the minimum weight W_{End} was taken to be 100%. In Fig. 1**f**, the three weight-loss stages could be observed, involving the loss of water molecules (30 – 130 ℃), the dehydroxylation of the Cr-O clusters and elimination of the monocarboxylate linkers (SO_3H-BDC) (350 – 500 ℃) (Hong et al., 2009), along with the collapse of skeleton (550 – 700 ℃) (Kayal et al., 2018). When the temperature was increased up to 700 °C, the continuous weight loss was observed, resulting from the cleaving of SO_3H-BDC linkers, in which the final product was determined as Cr_2O_3 (PXRD determination). According to the TGA results, the weight loss of SO_3H-MIL-101(Cr) and SS-SO_3H-MIL-101(Cr)− 3 in the last step was determined as 102.2 wt% and 85.1 wt%, respectively. Correspondingly, the coordination numbers of Cr-O cluster in SO_3H-MIL-101(Cr) and SS-SO_3H-MIL-101(Cr)− 3 were calculated as 4.08 and 3.40, respectively (the detailed calculation about the TGA results was given in SI, Section 3.1, Eqs. S1-**3**). Theoretically, each $[CrO_3(H_2O)_3]$ cluster in SO_3H-MIL-101(Cr) was coordinated and stabilized by six SO_3H-BDC linkers (Hong et al., 2009), indicating that partial linkers were missed during the post-treatment via seignette salt, and the structural defects were introduced into the SO_3H-MIL-101(Cr) (Zhang et al., 2021a). Furthermore, by comparing the N_2 adsorption-desorption isotherms of SO_3H-MIL-101(Cr) and series of SS-SO_3H-MIL-101(Cr)-X measured at 77 K, it is certain that the modification in the framework led to decreases in the Brunauer-Emmett-Teller (BET) surface area along with pore volume from 1049 $m^2 \cdot g^{-1}$ and 0.6 cm^3/g of the pristine SO_3H-MIL-101(Cr) to 547 $m^2 \cdot g^{-1}$ and 0.4 cm^3/g of the SS-SO_3H-MIL-101(Cr)− 4 (Fig. S2**,** Table S1). The declining specific surface area and pore volume as well as the increasing pore size could be ascribed to the ligands decomposition, which led to a partial pore collapse within the framework. The decrease in the crystallinity of SS-SO_3H-MIL-101(Cr)-X observed in the PXRD pattern also supported this result (Fig. 1**a**). Additionally, the seignete salt modulation expanded pore windows of SS-SO_3H-MIL-101(Cr)-X from 2.19 nm of the pristine SO_3H-MIL-101(Cr) to 2.22, 2.28 and 2.42 nm of SS-SO_3H-MIL-101(Cr)− 2, SS-SO_3H-MIL-101(Cr)− 3 and SS-SO_3H-MIL-101(Cr)− 4, promoting targeted metal cations diffusion from aqueous solution into functional spaces (Cai et al., 2021).

Overall, these results confirmed the successful preparation of defective SS-SO_3H-MIL-101(Cr)-X, in which the defect ratio could be regulated by the seignette salt concentrations. As illustrated in Scheme 1, among the modification process, the missing linkers in the structure of SS-SO_3H-MIL-101(Cr)-X could yield abundant oxygen vacancies, thereby providing the extra adsorption sites for capturing the cationic metal ions.

3.2. Adsorption performance

3.2.1. Adsorption performance towards lead ions

To explore the efficiency and capacity of SO_3H-MIL-101(Cr) and SS-SO_3H-MIL-101(Cr)-X toward cationic metal ions, the two critical parameters for adsorption kinetics, thermodynamics and isotherms were further determined (Eqs. S4-S12). Hereon, the lead ions (Pb^{2+}) were selected as a representative toxic metal cation to investigate the adsorption behavior of SO_3H-MIL-101(Cr) and SS-SO_3H-MIL-101(Cr)-X in aqueous solution (Zou et al., 2022). In Fig. 2**a**, the extremely fast adsorption kinetics (within 30 min) and superior adsorption capacities of modulated SS-SO_3H-MIL-101(Cr)-X toward Pb^{2+} (154.7, 160.4, 167.2 $mg \cdot g^{-1}$ of SS-SO_3H-MIL-101(Cr)− 2, SS-SO_3H-MIL-101(Cr)− 3, SS-SO_3H-MIL-101(Cr)− 4, respectively) were observed, in which the SS-SO_3H-MIL-101(Cr)− 3 was selected as the optimal adsorbent considering the superior adsorption capacity (Figs. S3–**4**), satisfied yield (Table S2) and acid stability (Fig. S5). The excellent adsorption performance can be ascribed to its sufficient active sites for interaction with the Pb^{2+} ions (Huang et al., 2022). The experimental data matched well with pseudo-second-order model (Fig. 2**a,** Table S3), implying that the Pb^{2+} adsorption processes involved chemical sorption (Aksu, 2001). As presented in Fig. 2**b**, the enhanced liquid film diffusion rate (K_I) in 1st stage (Table S3) might resulted from the creation of more Cr-O active sites (Li et al., 2021). Specifically, the internal diffusion rate (K_{II}) increased with the seignette salt concentration and followed the order of $K_{II} > K_I$, implying that the adsorption process over the adsorbent particle was mutually controlled by both film and intraparticle diffusion (Ahamad et al., 2018).

By fitting with Langmuir, Freundlich and Dubinin-Radushkevich (D-R) models under different temperatures, the Langmuir model exhibited a satisfactory fitting coefficient ($R^2 > 0.99$), indicating that the adsorption process of SS-SO_3H-MIL-101(Cr)− 3 toward Pb^{2+} might originate from a monolayer adsorption (Wu et al., 2019) (Fig. 2**c,** Table S4). The thermodynamic parameters of Pb^{2+} sorption over SS-SO_3H-MIL-101(Cr)− 3 were summarized in Table S5. And the corresponding plots of the Van't Hoff equation were illustrated in Fig. S6. More specifically, the as-calculated Gibbs free energy ΔG^o from − 29.36 to − 30.06 $kJ \cdot mol^{-1}$ indicated that the sorption was thermodynamically spontaneous process involving physical and chemical adsorption (Haque et al., 2014). The positive value of entropy change ΔS^o (35.12 $J \cdot mol^{-1} \cdot K^{-1}$) implied that the interface tended to be randomness during the sorption process (Haque et al., 2011), while the negative enthalpy change ΔH^o (−19.21 $kJ \cdot mol^{-1}$) implied that the sorption is the exothermic process (Haque et al., 2010).

For economical operation, the regeneration and reuse of the adsorbents is necessary. Five cycles of sorption and desorption experiments over SS-SO_3H-MIL-101(Cr)− 3 were conducted. As shown in Fig. 2**d,** the capture process can be retained for five successive cycles with removel efficiencies of over 95% for all the tested metal ions. Therein, the metal ions-loaded SS-SO_3H-MIL-101(Cr)− 3 can be regenerated by being centrifuged via the 1% HNO_3 solution, in which the leached chromium

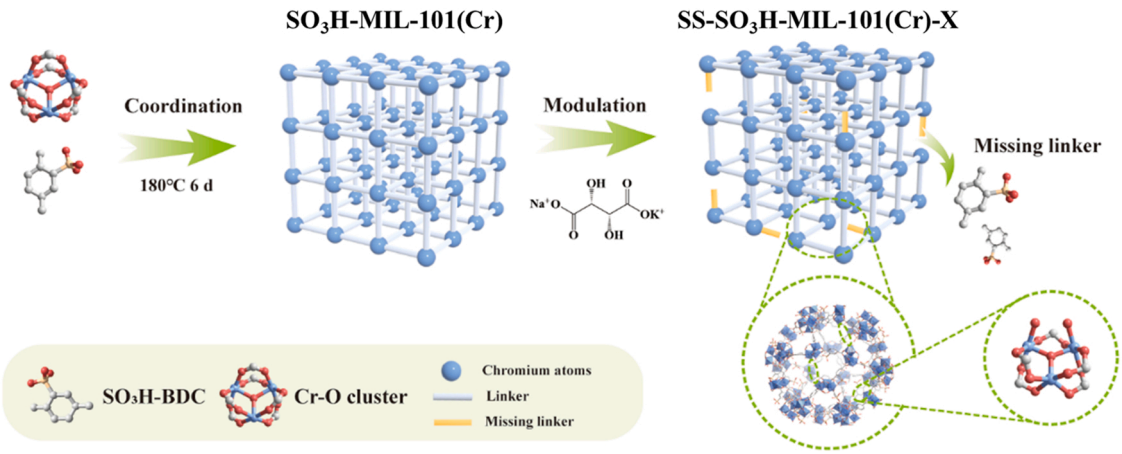

Scheme 1. The schematic illustration for pristine SO_3H-MIL-101(Cr) and defective SS-SO_3H-MIL-101(Cr)-X.

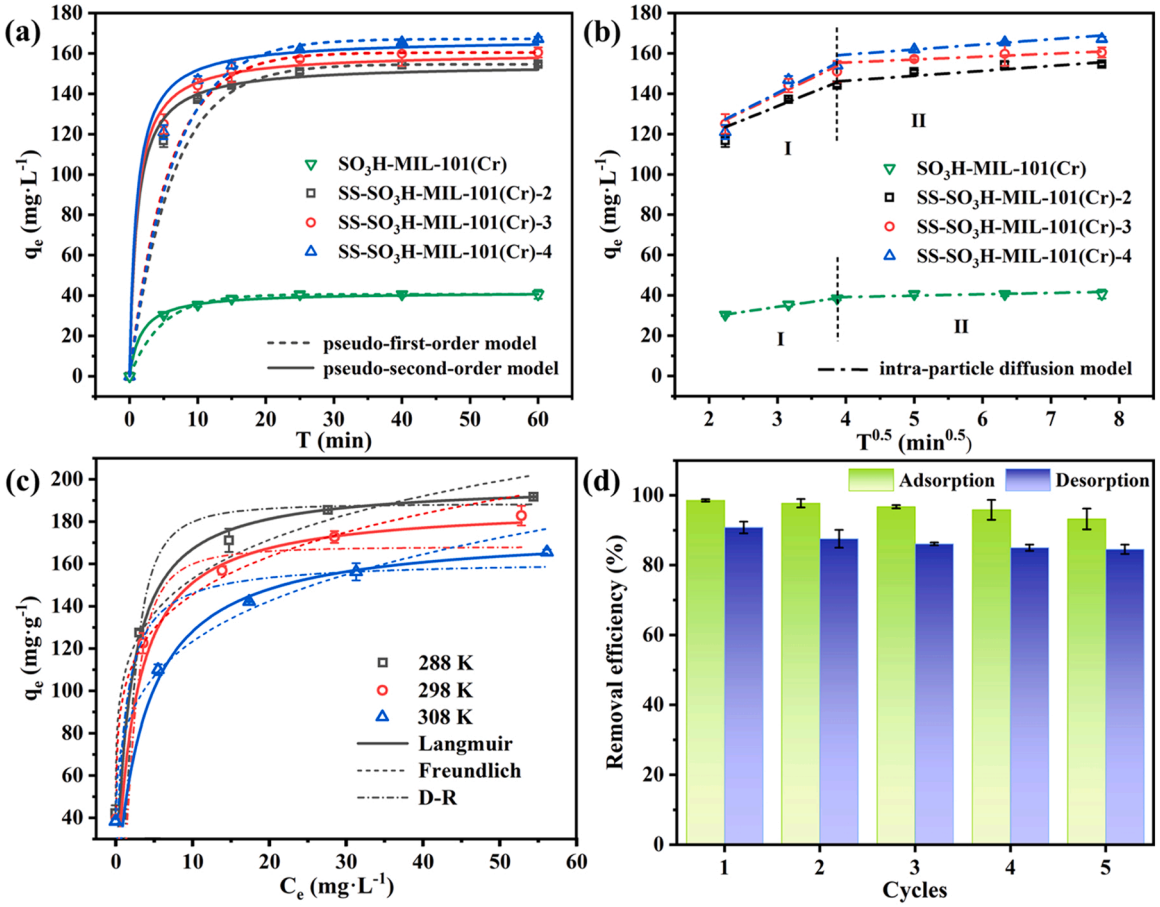

Fig. 2. (a) The pseudo-first-order, pseudo-second-order kinetics and (b) intra-particle diffusion models for sorption process of SO_3H-MIL-101(Cr) and series SS-SO_3H-MIL-101(Cr)-X towards Pb^{2+} (Experimental conditions: sorbent dose = 0.2 mg·mL^{-1}, $[Pb^{2+}]_0$ = 50 mg·L^{-1}, initial pH = 5.6, T = 25 ℃), (c) the Langmuir fitting of SS-SO_3H-MIL-101(Cr)− 3 for Pb^{2+} adsorption under different temperatures (Experimental conditions: sorbent dose = 0.2 mg·mL^{-1}, $[Pb^{2+}]_0$ = 50 mg·L^{-1}, initial pH = 5.6), (d) the cyclic stability experiments of the SS-SO_3H-MIL-101(Cr)− 3 (Experimental conditions: sorbent dose = 0.2 mg·mL^{-1}, $[Pb^{2+}]_0$ = 10 mg·L^{-1}, eluent: 1% HNO_3 solution, T = 25 ℃).

increased from 0.07 wt% to 0.45 wt% after five desorption cycles, attributing to the slight damage of framework by desorption agent (Fig. S7). Up to five cycles of Pb^{2+} adsorption-desorption performances affirmed the super stability of SS-SO_3H-MIL-101(Cr)− 3 in regeneration process.

3.2.2. *Adsorption performances of SS-SO_3H-MIL-101(Cr)-X toward different metal ions*

To explore the sorption performance of SS-SO_3H-MIL-101(Cr)-X toward various heavy metal cations, eight different kinds of metal ions like precious metals (Ag^+), toxic heavy metals (Pb^{2+}, Ba^{2+}, Cd^{2+}), radioactive metal ions (Cs^+, Sr^{2+}) and rare earth ions (Eu^{3+}, La^{3+}) were selected as target ions to be captured in the breakthrough processes.

As shown in Fig. 3**a**, SS-SO_3H-MIL-101(Cr)− 3 demonstrated excellent sorption performances toward all the selected metal ions, in which the removal efficiencies were over 99%. It's worth noting that the modulated SS-SO_3H-MIL-101(Cr)− 3 outperformed the pristine SO_3H-MIL-101(Cr) in all the metal cations capture tests, which exhibited superior adsorption activity toward Ag^+ and Pb^{2+} to the counterpart adsorbents (Fig. 3**b**, Table S6). The adsorption capacities of SS-SO_3H-MIL-101(Cr)− 3 toward different cations followed the order of Ag^+ (197.1 mg·g^{-1}) > Pb^{2+} (183.4 mg·g^{-1}) > Cs^+ (141.0 mg·g^{-1}) > Ba^{2+} (105.1 mg·g^{-1}) > Cd^{2+} (98.7 mg·g^{-1}) > Eu^{3+} (86.8 mg·g^{-1}) > Sr^{2+} (77.0 mg·g^{-1}) > La^{3+} (75.9 mg·g^{-1}). The differences in adsorption capacity could be explained by either the ionic radius, hydrated radius values or/and the hard/soft acid/base (HSAB) theory. As shown in Table S7, larger ionic radius and lower hydration energy of Cs^+ (0.17 nm, 264 kJ·mol^{-1}), Ba^{2+} (0.14 nm, 1250 kJ·mol^{-1}), Pb^{2+} (0.12 nm, 1502 kJ·mol^{-1}) and Ag^+ (0.13 nm, 474 kJ·mol^{-1}) favored the interaction with anionic SO_3H-MIL-101(Cr) and SS-SO_3H-MIL-101(Cr)− 3 (Nimbalkar et al., 2021). Moreover, according to the hard/soft acid/base (HSAB) theory, the sulfur containing groups in SO_3H-MIL-101(Cr) and SS-SO_3H-MIL-101(Cr)-X as soft base could readily bind with borderline acid of Pb^{2+} and soft acid of Ag^+ (Liu et al., 2020b). The fairly lower hydration energy and larger ionic radius of Ag^+ as well as its strong affinity with the sulfur containing group are responsible for its optimal adsorption capacity in aqueous solution.

The fixed-bed continuous adsorption experiments were employed to further exemplify the practicality of SS-SO_3H-MIL-101(Cr)− 3 for various metal cations adsorption (Fig. 3**c**). As shown in Fig. 3**d**, all the selected metal ions were effectively adsorbed by SS-SO_3H-MIL-101(Cr)− 3 with removal efficiencies > 99%. The breakthrough experiments of the packed bed of SS-SO_3H-MIL-101(Cr)− 3 toward the targeted solutions with flow rates of 5.0 mL·min^{-1} at room temperature demonstrated that the concentrations of all the selected metal ions in effluent were reduced from 5.0mg·L^{-1} to trace level (0.01–2.5 μg·L^{-1}). For Ba^{2+}, Cd^{2+} and Pb^{2+}, the effluent concentrations could satisfy the drinking water standards of world health organization (WHO) (Fig. S8). All the breakthrough curves increased sharply due to the rapid mass transfer and sorption kinetics (Bhaumik et al., 2013).

Furthermore, the adsorption abilities of SS-SO_3H-MIL-101(Cr)− 3 toward seven selected heavy metal ions were tested. In Fig. S9, SS-SO_3H-MIL-101(Cr)− 3 exhibited remarkable performance in capturing multiple metal cations synchronously with a removal efficiency of > 98%. All of the above exciting findings clearly indicated that SS-SO_3H-MIL-101(Cr)− 3, as a promising adsorbent for capturing multiple metal contaminants, may be of great value to practical applications.

3.3. Mechanistic insights of the adsorption

To further investigate the adsorption mechanism of SS-SO_3H-MIL-101(Cr)− 3 toward different heavy metal ions like Ag^+ (precious metal), Cs^+ (radioactive metal), Pb^{2+} (toxic heavy metal), Eu^{3+} (rare earth ion), a series of characterization and theoretical calculations were carried out. As illustrated in Fig. S10, the corresponding elemental mapping of SS-SO_3H-MIL-101(Cr)− 3 after adsorption revealed uniform distribution of the target metals, suggesting that the adsorption sites were evenly

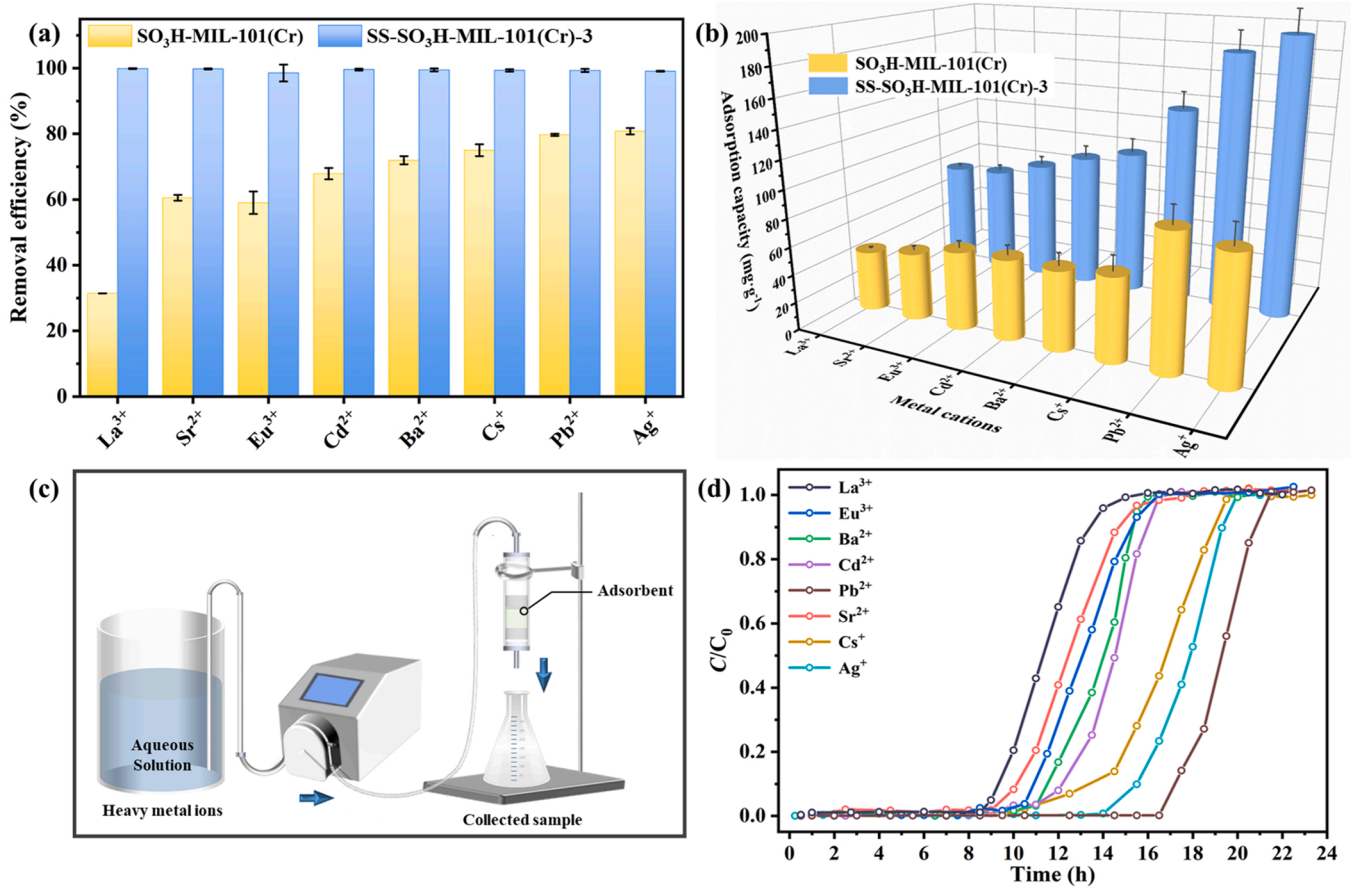

Fig. 3. (a) The removal efficiencies of SO_3H-MIL-101(Cr) and SS-SO_3H-MIL-101(Cr)− 3 towards different metal cations in single-component systems (Experimental conditions: sorbent dose = 0.2 mg·L^{-1}, initial concentration of the metal cation = 10 mg·L^{-1}, initial pH = 5.6, T = 25 ℃), (b) the adsorption capacities of SO_3H-MIL-101(Cr) and SS-SO_3H-MIL-101(Cr)− 3 for metal cations (Experimental conditions: sorbent dose = 0.2 mg·L^{-1}, initial concentration = 100 mg·L^{-1}, initial pH = 5.6, T = 25 ℃), (c) the schematic diagram of fixed-bed column apparatus and (d) breakthrough curves in the single component fixed-bed adsorption (Experimental conditions: sorbent dose = 0.3 g, initial concentration = 5 mg·mL^{-1}, initial pH = 5.6, T = 25 ℃, flow rate = 5 mL·min^{-1}).

distributed within the frameworks.

The obtained zeta potential values of SO_3H-MIL-101(Cr) and SS-SO_3H-MIL-101(Cr)− 3 were negative at the wide pH range, in which the zeta potentials decreased with the increase of pH (Fig. 4**a**). It was observed that the potentials of SO_3H-MIL-101(Cr) and SS-SO_3H-MIL-101(Cr)− 3 were − 15.7 mV and − 50.7 mV at pH = 6, respectively. Thus, the favorable adsorption of SS-SO_3H-MIL-101(Cr)− 3 toward cationic metal ions may be ascribed to the electrostatic interactions between the cationic metal ions and the negatively charged surface of SS-SO_3H-MIL-101(Cr)− 3 (Wang et al., 2015). This conjecture could be confirmed by the results that the maximum Pb^{2+} sorption capacity was achieved at pH = 6.0 (Fig. 4**b**). Furthermore, both SO_3H-MIL-101(Cr) and SS-SO_3H-MIL-101(Cr)− 3 exhibited satisfactory acid stability, in which the concentrations of leached total chromium ions from the adsorbents at pH range from 4.0 to 6.0 were below 100 $\mu g \cdot L^{-1}$ (0.05 wt%), which satisfied the standard of drinking water restricted by WHO (Pooja et al., 2019).

To further verify the key role of coordination interactions in the adsorption process, the XPS analyses were performed to check the chemical composition of SS-SO_3H-MIL-101(Cr)− 3 before and after metal cations uptake. The XPS spectra in Fig. 5**a** indicated that the metal cations were indeed adsorbed on the SS-SO_3H-MIL-101(Cr)− 3 solid. From the deconvolution spectrum of O 1 s (Fig. 5**b**), four peaks located at 532.34, 531.69, 533.03 and 531.15 eV could be assigned to Cr-O-C species, the S-O-H signal, C═O and carbon-hydroxyl (C-OH) on the adsorbed SS-SO_3H-MIL-101(Cr)− 3, respectively (Luo et al., 2017; Yu et al., 2021). The peak of S-O-H shifted from 531.69 eV of the fresh SS-SO_3H-MIL-101(Cr)− 3 to the higher binding energies after adsorption toward different cations (531.71 eV, 531.84 eV, 531.79 eV and 531.49 eV for SS-SO_3H-MIL-101(Cr)− 3-Ag, SS-SO_3H-MIL-101(Cr)− 3-Cs, SS-SO_3H-MIL-101(Cr)− 3-Pb, and SS-SO_3H-MIL-101(Cr)− 3-Eu, respectively), implying that the O atoms in the -SO_3H functional groups were interacted with the target metal cations (Jiang et al., 2021b). Meanwhile, the percentage of the Cr-OH peaks decreased from 26.32% to 15.66% (SS-SO_3H-MIL-101(Cr)− 3-Ag), 12.36% (SS-SO_3H-MIL-101(Cr)− 3-Cs), 5.99% (SS-SO_3H-MIL-101(Cr)− 3-Pb), 13.25% (SS-SO_3H-MIL-101(Cr)− 3-Eu); while the content of -O-C═O decreased from 27.95% to 16.13%, 14.20%, 22.80%, 15.47%, respectively, which might be assigned to the formed coordination between metal cations and the O atoms (Keshavarz et al., 2022). Correspondingly, the M-O peaks appeared after adsorption, further indicating that the adsorbates were coordinated with the hydroxyl groups, sulfonate groups and Cr-oxo clusters of SS-SO_3H-MIL-101(Cr)− 3 in the sorption process (Li et al., 2011; Liu et al., 2020a). Noticeably, it was observed that the Ag^0 element was formed over the adsorbent after Ag^+ uptake, which can be confirmed by the observations of Ag 3d peaks at 368.22 eV and 374.26 eV of SS-SO_3H-MIL-101(Cr)− 3-Ag (Zhou et al., 2020). It was demonstrated that partial silver ions adsorbed over the SS-SO_3H-MIL-101(Cr)− 3 were reduced to metallic Ag^0. Our previous researches also reported that electron-donating group like -OH could reduce Ag^+ to Ag^0 (Lu et al., 2015; Ren et al., 2022). This finding could be supported by the observed lattice fringe of ca. 0.234 nm corresponding to the (111) facet of Ag^0 in the high-resolution TEM (HRTEM) image (Fig. S11) (Wang et al., 2022c).

The density functional theory (DFT) calculations were employed to provide an in-depth investigation of the adsorption mechanism for SS-SO_3H-MIL-101(Cr)− 3 towards different metal cations at the molecular level. After modulation with seignette salt, the optimum geometric structures, adsorption energies (E_{ads}) and bond lengths of SS-SO_3H-MIL-101(Cr)− 3 for adsorbing target ions (Ag^+, Cs^+, Pb^{2+} and Eu^{3+}, as the computational models) at two possible interaction sites were shown in Fig. 6**a** (Eq. S13). The presence of missing linker defects induced the formation of oxygen vacancies in the framework, leading to the Cr-O-M coordination interactions (Model-1), while the S-O-M could be formed by the coordination between metal cations with sulfonic acid group (Model-2). Notably, the more negative the binding energy and shorter bond distance meant the stronger interaction between the metal-adsorbent complexes (Kim et al., 2021; Wang et al., 2020). As exhibited in Fig. 6**a**, the adsorbed metal cations were inclined to undergo Model-1 owing to its more negative binding energy (−35.61, −27.06, −18.96, −10.69 $kcal \cdot mol^{-1}$, respectively) than Model-2 (−20.31, −15.97, −10.26 and −8.65 $kcal \cdot mol^{-1}$, respectively), indicating that the Cr-O cluster played a dominant role in the complexation of metal cations onto SS-SO_3H-MIL-101(Cr)− 3. Furthermore, the corresponding bond lengths and binding energies indicated that the affinities toward these four metal cations were in the order of $Pb^{2+} > Ag^+ > Cs^+ > Eu^{3+}$ (Fig. 6**b**).

According to the above analyses, the parameters including crystal defect, pore volume, zeta potential and adsorption energy synergistically affect the adsorption properties of the adsorbents. As depicted in Fig. 7**a,** SS-SO_3H-MIL-101(Cr)− 3 with the most optimal crystal defects displayed more negative zeta potential and adsorption energy, along with the smaller pore volume. The existence of the defects introduced more adsorption sites into SS-SO_3H-MIL-101(Cr)− 3 framework. Among the adsorption process, the possible mechanism were electrostatic interactions (the first stage process) along with coordination interactions between metal cations and the O atoms from sulfonic acid group or unsaturated Cr-oxo clusters (the second stage process) (Fig. 7**b**).

4. Conclusion

In summary, the defective SS-SO_3H-MIL-101(Cr)-X had been

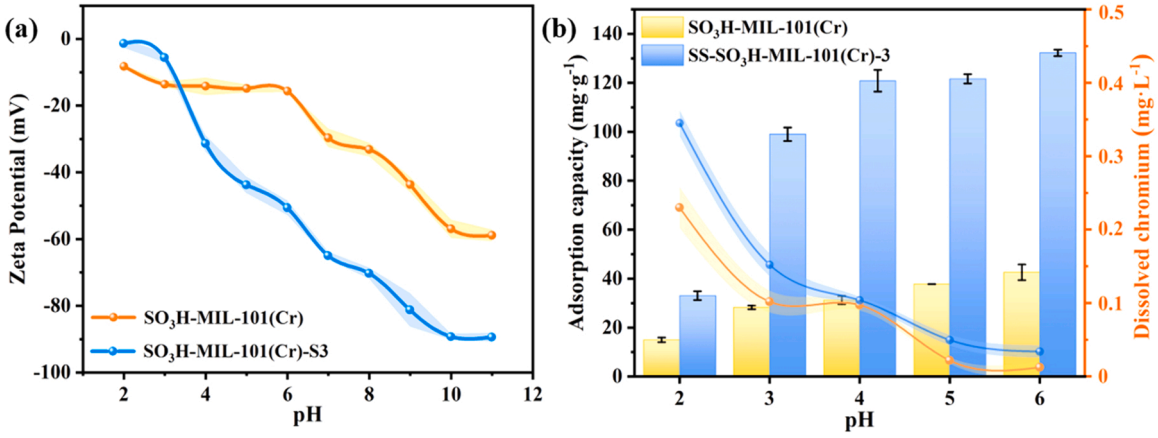

Fig. 4. (a) The zeta potential and (b) the sorption capacities of SO_3H-MIL-101(Cr) and SS-SO_3H-MIL-101(Cr)− 3 under different pHs (Experimental conditions: sorbent dose = 0.2 $mg \cdot mL^{-1}$, $[Pb^{2+}]_0$ = 50 $mg \cdot L^{-1}$, T = 25 °C).

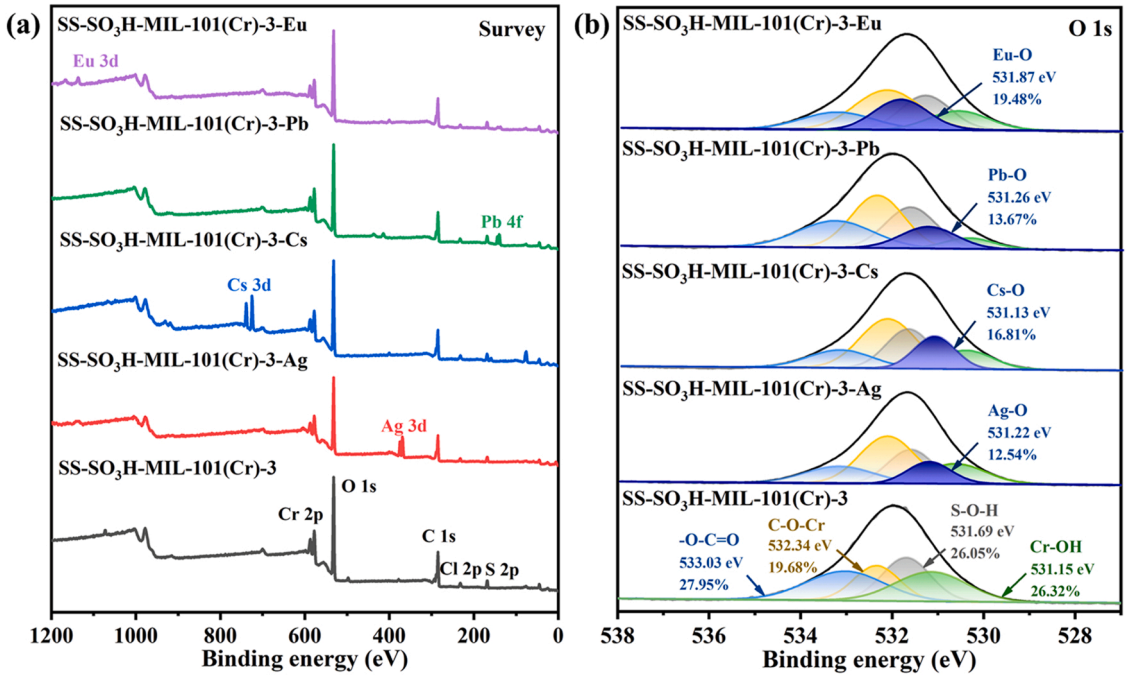

Fig. 5. Characterization of SS-SO_3H-MIL-101(Cr)− 3 before and after metal ion loading, (a) Wide-scan XPS spectra and (b) O 1 s.

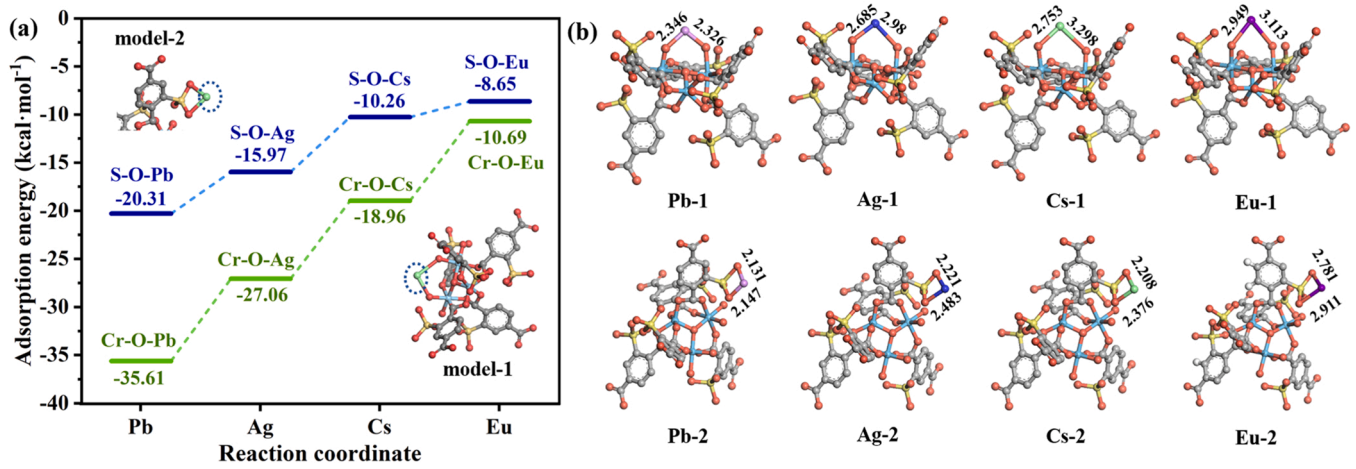

Fig. 6. (a) Calculated adsorption energy diagram, (b) DFT calculation models and structures for Ag^+, Cs^+, Pb^{2+} and Eu^{3+} adsorption onto SS-SO_3H-MIL-101(Cr)− 3. (Gray, red, yellow, blue, pink, mazarine, green and purple balls denote C, O, S, Cr, Pb, Ag, Cs and Eu atoms, respectively.).

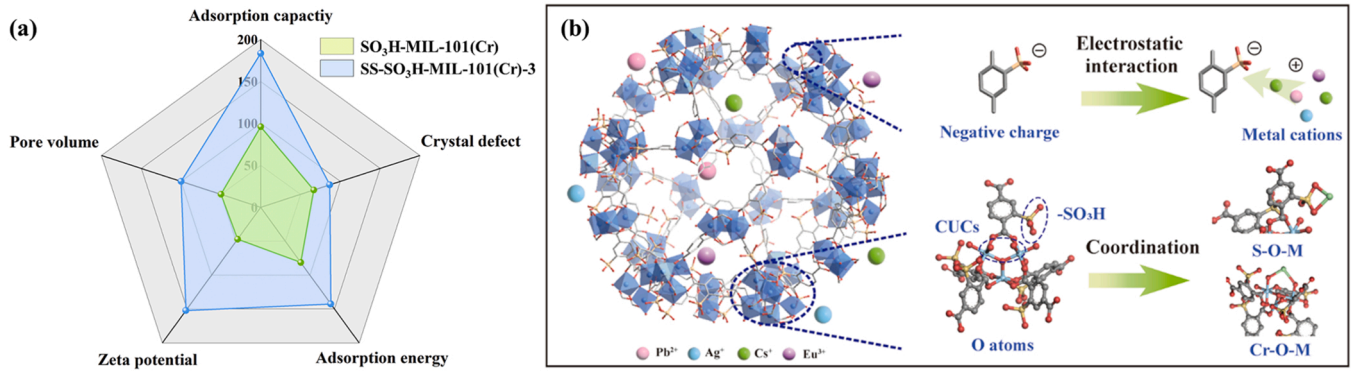

Fig. 7. (a) The diagram of the relationship between crystal defect, adsorption energy, zeta potential, pore volume and adsorbent performance of SO_3H-MIL-101(Cr) and SS-SO_3H-MIL-101(Cr)− 3, (b) the possible adsorption mechanism of SS-SO_3H-MIL-101(Cr)-X toward metal cations.

rationally designed via employing seignette salt. Due to the increased adsorption sites (oxygen vacancies), the adsorption capacity of as-prepared SS-SO_3H-MIL-101(Cr)-X toward eight kinds of metal cations exhibited significant improvement, with the nonspecifically capture efficiencies of > 99%. Notably, the breakthrough test revealed that the terminal concentrations of the multiple heavy metal ions were decreased from 5.0 ppm to extremely low levels (0.01–2.5 ppb). Furthermore, the XPS and DFT results affirmed that the uncoordinated oxygen on the Cr-O cluster and the O atoms in the -SO_3H functional groups played significant roles in the coordination during sorption process. The experimental and DFT computational results collaborative validated the mechanism of affinity difference of SS-SO_3H-MIL-101(Cr)-X toward disparate cations. Especially, the optimal SS-SO_3H-MIL-101(Cr)− 3 exhibited satisfactory Pb^{2+} adsorption capacity (189.6 $mg{\cdot}g^{-1}$) and excellent desorption recirculation performance (removal efficiencies > 95% after 5 cycles) as well as the desirable stability (less than 100 $\mu g{\cdot}L^{-1}$ of Cr leaching under weak acidic conditions). This work provided an intriguing example of preparing defective Cr-based MOF adsorbent, in which the metal cation capture performance was boosted via the addition of adsorption sites to facilitate the potential application for industrial wastewater treatment.

Environmental implication

Toxic heavy metals were considered be detrimental to the environment and public health due to their teratogenic, carcinogenic, and mutagenic properties. In this work, the defective SO_3H-MIL-101(Cr) (SS-SO_3H-MIL-101(Cr)-X, X is the dosage of modulating agent seignette salt (SS)) with enhanced vacancies was fabricated to capture different heavy metal ions, including Ag^{+}, Cs^{+}, Pb^{2+}, Cd^{2+}, Ba^{2+}, Sr^{2+}, Eu^{3+} and La^{3+}. The optimal SS-SO_3H-MIL-101(Cr)− 3 could remove all the selected metal cations to below the permissible limits required by the WHO in the continuous-flow water treatment system. This work provided a good example for modulating SS-SO_3H-MIL-101(Cr)-X to promote its potential application in widespread metal cations removal from wastewater.

CRediT authorship contribution statement

Xueying Ren: Data curation, Investigation, Visualization, Writing - original draft. **Chong-Chen Wang:** Conceptualization, Funding acquisition, Supervision, Project administration, Writing - review & editing. **Ya Li**: Data curation, Software. **Peng Wang:** Resources, Instrumental. **Shijie Gao:** Methodology, Instrumental.

Declaration of Competing Interest

The authors declare that they have no known competing financial interests or personal relationships that could have appeared to influence the work reported in this paper.

Data availability

Data will be made available on request.

Acknowledgments

This work was supported by National Natural Science Foundation of China (5187802), Beijing Talent Project (2020A27), Young Teachers' Research Ability Enhancement Program for Beijing University of Civil Engineering and Architecture (X21085) and BUCEA Post Graduate Innovation Project (2022).

Appendix A. Supporting information

Supplementary data associated with this article can be found in the online version at doi:10.1016/j.jhazmat.2022.130552.

References

Ahamad, K., Singh, R., Baruah, I., Choudhury, H., Sharma, M., 2018. Equilibrium and kinetics modeling of fluoride adsorption onto activated alumina, alum and brick powder. Groundw. Sustain. Dev. 7, 452–458.
Aksu, Z., 2001. Equilibrium and kinetic modelling of cadmium (II) biosorption by C. vulgaris in a batch system: effect of temperature. Sep. Purif. Technol. 21, 285–294.
Bhaumik, M., Setshedi, K., Maity, A., Onyango, M.S., 2013. Chromium (VI) removal from water using fixed bed column of polypyrrole/Fe_3O_4 nanocomposite. Sep. Purif. Technol. 110, 11–19.
Bolisetty, S., Peydayesh, M., Mezzenga, R., 2019. Sustainable technologies for water purification from heavy metals: review and analysis. Chem. Soc. Rev. 48, 463–487.
Cai, G., Yan, P., Zhang, L., Zhou, H.-C., Jiang, H.-L., 2021. Metal–organic framework-based hierarchically porous materials: Synthesis and applications. Chem. Rev. 121, 12278–12326.
Chang, Z., Zeng, L., Sun, C., Zhao, P., Wang, J., Zhang, L., Zhu, Y., Qi, X., 2021. Adsorptive recovery of precious metals from aqueous solution using nanomaterials–A critical review. Coord. Chem. Rev. 445, 214072.
Chen, Q., Wang, M.-M., Hu, X., Chen, X.-W., Wang, J.-H., 2016. An octamolybdate-metal organic framework hybrid for the efficient adsorption of histidine-rich proteins. J. Mater. Chem. B 4, 6812–6819.
Du, X.-D., Wang, C.-C., Zhong, J., Liu, J.-G., Li, Y.-X., Wang, P., 2017. Highly efficient removal of Pb^{2+} by a polyoxomolybdate-based organic-inorganic hybrid material $\{(4\text{-Hap})_4[Mo_8O_{26}]\}$. J. Environ. Chem. Eng. 5, 1866–1873.
El Samrani, A., Lartiges, B., Villiéras, F., 2008. Chemical coagulation of combined sewer overflow: heavy metal removal and treatment optimization. Water Res 42, 951–960.
Férey, G., Mellot-Draznieks, C., Serre, C., Millange, F., Dutour, J., Surblé, S., Margiolaki, I., 2005. A chromium terephthalate-based solid with unusually large pore volumes and surface area. Science 309, 2040–2042.
Gao, M., Liu, G., Gao, Y., Chen, G., Huang, X., Xu, X., Wang, J., Yang, X., Xu, D., 2021. Recent advances in metal-organic frameworks/membranes for adsorption and removal of metal ions. TrAC, Trends Anal. Chem. 137, 116226.
Guan, X., Wang, Y., Cai, W., 2019. A composite metal-organic framework material with high selective adsorption for dibenzothiophene. Chin. Chem. Lett. 30, 1310–1314.
Guo, X., Kang, C., Huang, H., Chang, Y., Zhong, C., 2019. Exploration of functional MOFs for efficient removal of fluoroquinolone antibiotics from water. Microporous Mesoporous Mater. 286, 84–91.
Hadi, P., To, M.-H., Hui, C.-W., Lin, C.S.K., McKay, G., 2015. Aqueous mercury adsorption by activated carbons. Water Res 73, 37–55.
Haque, E., Lee, J.E., Jang, I.T., Hwang, Y.K., Chang, J.-S., Jegal, J., Jhung, S.H., 2010. Adsorptive removal of methyl orange from aqueous solution with metal-organic frameworks, porous chromium-benzenedicarboxylates. J. Hazard. Mater. 181, 535–542.
Haque, E., Jun, J.W., Jhung, S.H., 2011. Adsorptive removal of methyl orange and methylene blue from aqueous solution with a metal-organic framework material, iron terephthalate (MOF-235.). J. Hazard. Mater. 185, 507–511.
Haque, E., Lo, V., Minett, A.I., Harris, A.T., Church, T.L., 2014. Dichotomous adsorption behaviour of dyes on an amino-functionalised metal–organic framework, amino-MIL-101(Al). J. Mater. Chem. A 2, 193–203.
He, W., Ai, K., Ren, X., Wang, S., Lu, L., 2017. Inorganic layered ion-exchangers for decontamination of toxic metal ions in aquatic systems. J. Mater. Chem. A 5, 19593–19606.
Hong, D.Y., Hwang, Y.K., Serre, C., Ferey, G., Chang, J.S., 2009. Porous chromium terephthalate MIL-101 with coordinatively unsaturated sites: surface functionalization, encapsulation, sorption and catalysis. Adv. Funct. Mater. 19, 1537–1552.
Huang, Z., Xiong, C., Ying, L., Wang, W., Wang, S., Ding, J., Lu, J., 2022. A post-functional Ti-based MOFs composite for selective removal of Pb(II) from water. J. Hazard. Mater. 432, 128700.
Jiang, D., Huang, C., Zhu, J., Wang, P., Liu, Z., Fang, D., 2021a. Classification and role of modulators on crystal engineering of metal organic frameworks (MOFs). Coord. Chem. Rev. 444, 214064.
Jiang, W., Cui, W.-R., Liang, R.-P., Qiu, J.-D., 2021b. Difunctional covalent organic framework hybrid material for synergistic adsorption and selective removal of fluoroquinolone antibiotics. J. Hazard. Mater. 413, 125302.
Kabtamu, D.M., Wu, Y.-n, Li, F., 2020. Hierarchically porous metal–organic frameworks: synthesis strategies, structure (s), and emerging applications in decontamination. J. Hazard. Mater. 397, 122765.
Kayal, S., Chakraborty, A., 2018. Activated carbon (type Maxsorb-III) and MIL-101 (Cr) metal organic framework based composite adsorbent for higher CH_4 storage and CO_2 capture. Chem. Eng. J. 334, 780–788.
Keshavarz, F., Kavun, V., van der Veen, M.A., Repo, E., Barbiellini, B., 2022. Molecular-level understanding of highly selective heavy rare earth element uptake by organophosphorus modified MIL-101(Cr). Chem. Eng. J. 440, 135905.
Kim, H.J., Choi, H., Sharma, A.K., Hong, W.G., Shin, K., Song, H., Kim, H.Y., Hong, Y.J., 2021. Recyclable aqueous metal adsorbent: Synthesis and Cu(II) sorption characteristics of ternary nanocomposites of Fe_3O_4 nanoparticles@ graphene–poly-N-phenylglycine nanofibers. J. Hazard. Mater. 401, 123283.
Kobielska, P.A., Howarth, A.J., Farha, O.K., Nayak, S., 2018. Metal–organic frameworks for heavy metal removal from water. Coord. Chem. Rev. 358, 92–107.
Li, J., Chen, S., Sheng, G., Hu, J., Tan, X., Wang, X., 2011. Effect of surfactants on Pb (II) adsorption from aqueous solutions using oxidized multiwall carbon nanotubes. Chem. Eng. J. 166, 551–558.
Li, M., Liu, Y., Li, F., Shen, C., Kaneti, Y.V., Yamauchi, Y., Yuliarto, B., Chen, B., Wang, C.-C., 2021. Defect-rich hierarchical porous uio-66 (zr) for tunable phosphate removal. Environ. Sci. Technol. 55, 13209–13218.

Li, Y.-H., Wang, C.-C., Zeng, X., Sun, X.-Z., Zhao, C., Fu, H., Wang, P., 2022a. Seignette salt induced defects in Zr-MOFs for boosted Pb(II) adsorption: universal strategy and mechanism insight. Chem. Eng. J. 442, 136276.

Li, Y.-H., Wang, P., Wang, C.-C., Y.B, L., 2022b. State-of-the-art review of defective metal-organic frameworks for pollutant removal from water. Chin. J. Inorg. Chem. https://doi.org/10.11862/CJIC.2022.252.

Liu, J., Li, X., Han, Y., Wu, J., Zhang, X., Wang, Z., Xu, Y., 2020a. Synergetic effect of tetraethylammonium bromide addition on the morphology evolution and enhanced photoluminescence of rare-earth metal–organic frameworks. Inorg. Chem. 59, 14318–14325.

Liu, Q., Li, S., Yu, H., Zeng, F., Li, X., Su, Z., 2020b. Covalently crosslinked zirconium-based metal-organic framework aerogel monolith with ultralow-density and highly efficient Pb(II) removal. J. Colloid Interface Sci. 561, 211–219.

Llanos, J., Williams, P., Cheng, S., Rogers, D., Wright, C., Perez, A., Canizares, P., 2010. Characterization of a ceramic ultrafiltration membrane in different operational states after its use in a heavy-metal ion removal process. Water Res. 44, 3522–3530.

Lu, Q., Deng, J., Hou, Y., Wang, H., Li, H., Zhang, Y., Yao, S., 2015. Hydroxyl-rich C-dots synthesized by a one-pot method and their application in the preparation of noble metal nanoparticles. Chem. Commun. 51, 7164–7167.

Luo, X.-P., Fu, S.-Y., Du, Y.-M., Guo, J.-Z., Li, B., 2017. Adsorption of methylene blue and malachite green from aqueous solution by sulfonic acid group modified MIL-101. Microporous Mesoporous Mater. 237, 268–274.

Ma, J., Wang, C.-C., Zhao, Z.-X., Wang, P., Li, J.-J., Wang, F.-X., 2021. Adsorptive capture of perrhenate (ReO_4^-) from simulated wastewater by cationic 2D-MOF BUC-17. Polyhedron 202, 115218.

Mortazavi, S.S., Abbasi, A., Masteri-Farahani, M., Farzaneh, F., 2019. Sulfonic acid functionalized MIL-101 (Cr) metal-organic framework for catalytic production of acetals. ChemistrySelect 4, 7495–7501.

Nakhjiri, A.T., Sanaeepur, H., Amooghin, A.E., Shirazi, M.M.A., 2022. Recovery of precious metals from industrial wastewater towards resource recovery and environmental sustainability: a critical review. Desalination 527, 115510.

Navarro, R.R., Wada, S., Tatsumi, K., 2005. Heavy metal precipitation by polycation–polyanion complex of PEI and its phosphonomethylated derivative. J. Hazard. Mater. 123, 203–209.

Nimbalkar, M.N., Bhat, B.R., 2021. Simultaneous adsorption of methylene blue and heavy metals from water using Zr-MOF having free carboxylic group. J. Environ. Chem. Eng. 9, 106216.

Peng, Y., Huang, H., Zhang, Y., Kang, C., Chen, S., Song, L., Liu, D., Zhong, C., 2018. A versatile MOF-based trap for heavy metal ion capture and dispersion. Nat. Commun. 9, 1–9.

Pooja, D., Singh, L., Thakur, A., Kumar, P., 2019. Green synthesis of glowing carbon dots from Carica papaya waste pulp and their application as a label-freechemo probe for chromium detection in water. Sens. Actuators, B 283, 363–372.

Ran, Z., Liu, J., Mushtaq, M.A., Shao, X., Liu, H., Du, X., Hou, S., Ji, S., 2022. Preparation of magnetic Au/MIL-101(Cr)@SiO_2@Fe_3O_4 catalysts and N-methylation reaction mechanism of CO_2 with aniline/H_2. Catal. Today. https://doi.org/10.1016/j.cattod.2022.04.017.

Ren, X., Wang, C.-C., Li, Y., Wang, C.-Y., Wang, P., Gao, S., 2022. Ag (I) removal and recovery from wastewater adopting NH_2-MIL-125 as efficient adsorbent: A 3Rs (reduce, recycle and reuse) approach and practice. Chem. Eng. J. 442, 136306.

Rychkov, V., Kirillov, E., Kirillov, S., Bunkov, G., Botalov, M., Semenishchev, V., Smyshlyaev, D., Malyshev, A., Taukin, A., Akcil, A., 2021. Rare earth element preconcentration from various primary and secondary sources by polymeric ion exchange resins. Sep. Purif. Rev. 51, 1–16.

Suksabye, P., Thiravetyan, P., 2012. Cr(VI) adsorption from electroplating plating wastewater by chemically modified coir pith. J. Environ. Manag 102, 1–8.

Sun, X., Xia, Q., Zhao, Z., Li, Y., Li, Z., 2014. Synthesis and adsorption performance of MIL-101 (Cr)/graphite oxide composites with high capacities of n-hexane. Chem. Eng. J. 239, 226–232.

Ullah, S., Akram, B., Ali, H., Zhang, H., Yang, H., Liu, Q., Wang, X., 2019. 2-Methylimidazole assisted ultrafast synthesis of carboxylate-based metal–organic framework nano-structures in aqueous medium at room temperature. Sci. Bull. 64, 1103–1109.

Wang, C., Lin, G., Zhao, J., Wang, S., Zhang, L., Xi, Y., Li, X., Ying, Y., 2020. Highly selective recovery of Au (III) from wastewater by thioctic acid modified Zr-MOF: Experiment and DFT calculation. Chem. Eng. J. 380, 122511.

Wang, C.-C., Ren, X., Wang, P., Chang, C., 2022a. The state of the art review on photocatalytic Cr (VI) reduction over MOFs-based photocatalysts: From batch experiment to continuous operation. Chemosphere 303, 134949.

Wang, C.-Y., Ma, L., Wang, C.-C., Wang, P., Gutierrez, L., Zheng, W., 2022b. Light-response adsorption and desorption behaviors of metal–organic frameworks. Environ. Funct. Mater. 1, 49–66.

Wang, F., Lu, X., Li, X.-y, 2016. Selective removals of heavy metals (Pb^{2+}, Cu^{2+}, and Cd^{2+}) from wastewater by gelation with alginate for effective metal recovery. J. Hazard. Mater. 308, 75–83.

Wang, X., Li, M., Xu, P., Chen, Y., Yu, H., Li, X., 2022c. In situ TEM technique revealing the deactivation mechanism of bimetallic Pd–Ag nanoparticles in hydrogen sensors. Nano Lett. 22 (7), 3157–3164.

Wang, Y., Ye, G., Chen, H., Hu, X., Niu, Z., Ma, S., 2015. Functionalized metal–organic framework as a new platform for efficient and selective removal of cadmium (II) from aqueous solution. J. Mater. Chem. A 3, 15292–15298.

Wu, B., Wan, J., Zhang, Y., Pan, B., Lo, I.M., 2019. Selective phosphate removal from water and wastewater using sorption: process fundamentals and removal mechanisms. Environ. Sci. Technol. 54, 50–66.

Yoo, D.K., Lee, G., Mondol, M.M.H., Lee, H.J., Kim, C.M., Jhung, S.H., 2023. Preparation and applications of metal–organic frameworks composed of sulfonic acid. Coord. Chem. Rev. 474, 214868.

Younis, S.A., Bhardwaj, N., Bhardwaj, S.K., Kim, K.-H., Deep, A., 2021. Rare earth metal–organic frameworks (RE-MOFs): Synthesis, properties, and biomedical applications. Coord. Chem. Rev. 429, 213620.

Yu, F., Song, F., Wang, R., Xu, M., Luo, F., 2021. Sulfonated perylene-based conjugated microporous polymer as a high-performance adsorbent for photo-enhanced uranium extraction from seawater. Polym. Chem. 12, 867–875.

Zhang, A., Liu, B., Liu, M., Xie, Z., Wang, D., Feng, G., 2021a. The adsorption properties of defect controlled metal-organic frameworks of UiO-66. Sep. Purif. Technol. 270, 118842.

Zhang, W., Huang, W., Jin, J., Gan, Y., Zhang, S., 2021b. Oxygen-vacancy-mediated energy transfer for singlet oxygen generation by diketone-anchored MIL-125. Appl. Catal., B 292, 120197.

Zhao, H., Zhao, X., Gao, Z., Liu, D., 2018. Effective removal of naphthalenesulfonic acid from water using functionalized metal–organic frameworks. J. Chem. Eng. Data 63, 3061–3067.

Zhao, Q., Yi, X.-H., Wang, C.-C., Wang, P., Zheng, W., 2022. Photocatalytic Cr (VI) reduction over MIL-101 (Fe)–NH_2 immobilized on alumina substrate: From batch test to continuous operation. Chem. Eng. J. 429, 132497.

Zhou, Y.-C., Wang, P., Fu, H., Zhao, C., Wang, C.-C., 2020. Ternary Ag/Ag_3PO_4/MIL-125-NH_2 Z-scheme heterojunction for boosted photocatalytic Cr (VI) cleanup under visible light. Chin. Chem. Lett. 31, 2645–2650.

Zhou, Y.-X., Chen, Y.-Z., Hu, Y., Huang, G., Yu, S.-H., Jiang, H.-L., 2014. MIL-101-SO_3H: a highly efficient Brönsted acid catalyst for heterogeneous alcoholysis of epoxides under ambient conditions. Chem. Eur. J. 20, 14976–14980.

Zorainy, M.Y., Alalm, M.G., Kaliaguine, S., Boffito, D.C., 2021. Revisiting the MIL-101 metal–organic framework: design, synthesis, modifications, advances, and recent applications. J. Mater. Chem. A 9, 22159–22217.

Zou, Y.-M., Ma, W., Sun, H.-Y., Tang, J.-H., Lv, T.-T., Feng, M.-L., Huang, X.-Y., 2022. High-capacity recovery of Cs^+ ions by facilely synthesized layered vanadyl oxalatophosphates with the clear insight into remediation mechanism. J. Hazard. Mater. 434, 128869.